Observation of Electrically-Inactive Interstitials in Nb-Doped $SrTiO_3$

Jong Seok Jeong,* Palak Ambwani, Bharat Jalan, Chris Leighton, and K. Andre Mkhoyan*

Department of Chemical Engineering and Materials Science, University of Minnesota, Minneapolis, Minnesota 55455, United States

ABSTRACT Despite rapid recent progress, controlled dopant incorporation and attainment of high mobility in thin films of the prototypical complex oxide semiconductor $SrTiO_3$ remain problematic. Here, analytical scanning transmission electron microscopy is used to study the local atomic and electronic structure of Nb-doped $SrTiO_3$ both in ideally substitutionally doped bulk single crystals and epitaxial thin films. The films are deposited under conditions that would yield highly stoichiometric *undoped* $SrTiO_3$, but are nevertheless insulating. The Nb incorporation in such films was found to be highly inhomogeneous on nanoscopic length-scales, with large quantities of what we deduce to be interstitial Nb. Electron energy loss spectroscopy reveals changes in the electronic density of states in Nb-doped $SrTiO_3$ films compared to undoped $SrTiO_3$, but without the clear shift in the Fermi edge seen in bulk single crystal Nb-doped $SrTiO_3$. Analysis of atomic-resolution annular dark-field images allows us to conclude that the interstitial Nb is in the Nb^0 state, confirming that it is electrically inactive. We argue that this approach should enable future work establishing the vitally needed relationships between synthesis/processing conditions and electronic properties of Nb-doped $SrTiO_3$ thin films.

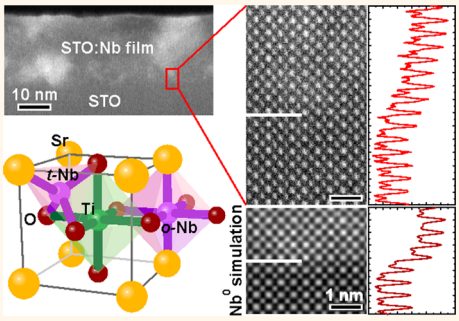

KEYWORDS: complex oxides · $SrTiO_3$ · doping · interstitials · STEM/EELS

$SrTiO_3$ (STO) is a model complex oxide semiconductor with such remarkable electronic properties that it has sustained attention for over five decades in bulk single crystal form. The quantum paraelectricity displayed by this material leads to formation of an anomalously low density high mobility metallic state,[1] provides access to quantum transport in a highly unusual limit,[2] and supports the most dilute superconducting state known.[3] The recent growth of interest in complex oxide heterostructures has further increased the appeal of this material. Two-dimensional (2D) electron systems have been created at heterointerfaces[4] and in delta-doped layers,[5,6] producing quantum oscillations[5,6] and 2D superconductivity.[5] Suggestions of emergent ferromagnetism have even been made in STO films,[7−9] while mobilities have been strain-enhanced beyond bulk crystals, reaching 120 000 $cm^2\ V^{-1}\ s^{-1}$.[10]

It is remarkable that this rapid progress has been possible given the difficulties encountered with controlled doping of STO films. In bulk crystals, *n*-type doping *via* O vacancies (in $SrTiO_{3-\delta}$), Nb substitution (in $SrTi_{1-y}Nb_yO_3$), and La substitution (in $Sr_{1-x}La_xNbO_3$) are all relatively well controlled [*e.g.*, ref 1]. Doping STO films and heterostructures has proven far more challenging, however, as the demands placed on crystalline perfection, stoichiometry, and defect density are severe. With commonly employed pulsed laser deposition (PLD) methods, incorporation of Nb dopants for example is nontrivial, and even when successful typically leads to mobilities far lower than bulk crystals. Recent work has provided important breakthroughs, however, including molecular beam epitaxy (MBE) growth of such highly stoichiometric films that single-crystal-like mobilities occur,[11] and deposition of precisely defect-managed PLD films with dramatically improved mobility.[12] Nevertheless, much remains to be understood regarding doping in *n*-STO, including the defects that limit the mobility, the mechanisms by which nonstoichiometry hinders dopant incorporation, and the local state of electrically inactive dopants.

In our own recent work, we have established (see Supporting Information) that carefully executed high pressure oxygen sputter deposition, much like precisely

* Address correspondence to jsjeong@umn.edu, mkhoyan@umn.edu.

Received for review March 4, 2013 and accepted April 27, 2013.

Published online April 28, 2013
10.1021/nn401101y

controlled PLD and MBE, is also capable of synthesis of highly stoichiometric undoped STO epilayers. Optimized deposition conditions lead to identical lattice parameters for film and substrate in homoepitaxy, in addition to vanishing interfacial contrast in X-ray scattering, two of the most stringent stoichiometry criteria.[11−13] Nevertheless, when these growth conditions are used for deposition of STO:Nb, we observe no measurable conductivity and significantly expanded out-of-plane lattice parameter (see Supporting Information), indicating electrically inactive dopants and significant nonstoichiometry. In this work, we show, by combining high-resolution X-ray diffraction (XRD), multiple modes of transmission electron microscopy (TEM), energy dispersive X-ray spectroscopy (EDX), and electron energy loss spectroscopy (EELS), that such films must in fact contain significant levels of interstitial Nb. This interstitial Nb is found to be inhomogeneously distributed within the films, creating local lattice strain, modifying the local electronic density of states (DOS), but not significantly doping electrons to the conduction band. We propose that the methods developed here could enable critical advances in understanding the doping problem in STO, most notably a full appreciation of how deposition and processing conditions can be optimized to promote fully electrically active substitutional doping.

RESULTS AND DISCUSSION

The results from one of the EDX experiments are presented in Figure 1, which shows the lateral variations in scanning TEM (STEM) low-angle annular dark-field (LAADF) intensity, Nb, Ti, O, and Sr EDX signal, and corresponding representative LAADF, Nb, Ti, O, and Sr images in a STO:Nb epilayer on STO(001). The EDX signals from the film were compared to those in the substrate. The thickness differences between film and substrate were also measured, using ADF intensities, and corresponding adjustments were made. The data reveal quite clearly that: (i) there are regions in the film where anomalously high concentration of Nb is observed, (ii) these regions are associated with higher LAADF intensity and lower Ti content, and (iii) there are no systematic variations in O or Sr content throughout the film. While the average LAADF intensity in the STO:Nb film is only marginally higher than that from the substrate, the local intensity variations are significant, and are correlated with the variations in Nb content. The Pearson correlation coefficient[14] between LAADF and Nb EDX intensities was evaluated at 0.85, confirming a strong correlation. This coefficient is −0.57 between the Nb and Ti signals (a relatively weak anticorrelation), suggesting that the excess Nb does not simply occupy vacant Ti sites. The Pearson coefficients for Sr/Ti and Sr/Nb are −0.38 and 0.72, respectively, with the Sr signal mostly varying around zero

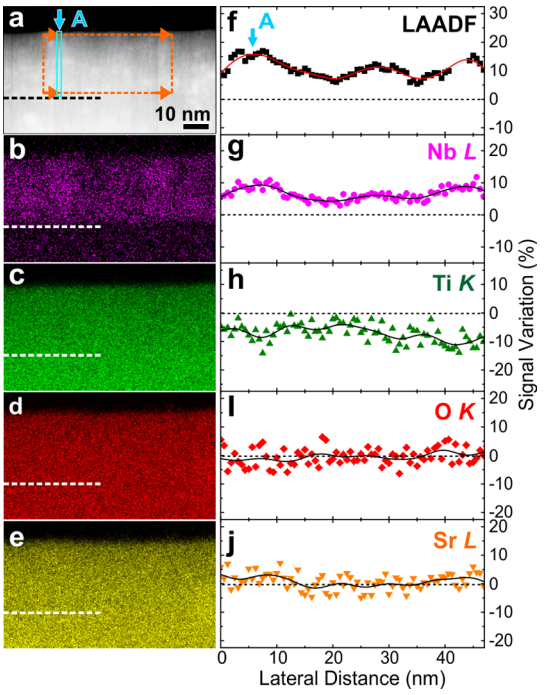

Figure 1. (a) STEM LAADF image of a STO:Nb film grown on a STO(001) substrate and corresponding EDX maps of Nb *L* (b), Ti *K* (c), O *K* (d), and Sr *L* (e) peaks recorded in parallel. The horizontal dotted lines indicate the interface between the film (top) and the substrate (bottom). Panels f−j show vertically averaged signal variations obtained from the region of the film indicated by the dotted rectangle in panel a. The LAADF, Ti, O, and Sr signals were normalized to the undoped STO substrate. The solid lines in the LAADF and EDX profiles are guides to the eye obtained by FFT-filter-smoothing to remove high frequency noise. The same parameters were used for all signals.

suggesting that there are no considerable or systematic changes in Sr content. There is no anticorrelation between Sr and Nb, and thus, the possibility of systematic presence of Nb on Sr lattice sites can apparently be ruled out. Since there are no correlated or systematic variations in the O signal and no secondary phase formation (see below), excess Nb (relative to deficient Ti) is expected to occupy interstitial sites, in addition to substituting for Ti. This point will be returned to throughout this paper. As an example of the magnitudes involved, the local composition of Nb and the fraction of interstitial Nb were evaluated in an example region. If all Ti losses are substituted by Nb, the excess Nb must be in the interstitial sites. In the region A in Figure 1 for example, the Ti loss is about 8.6 at. %, whereas the concentration of Nb is about 11.5 at. %, which means that about 2.9 at. % Nb (or 25% of the local Nb) is in interstitial sites. Since the loss of Ti atoms in the film is not uniform, the doped Nb substituting Ti must also be clustered. As returned to below, this dopant clustering may well play a significant role in limiting electrical conduction in these films.

The visible increase in STEM ADF signal in the high Nb content regions could be attributed either to changes in composition[15,16] or to the presence of strain.[17] While

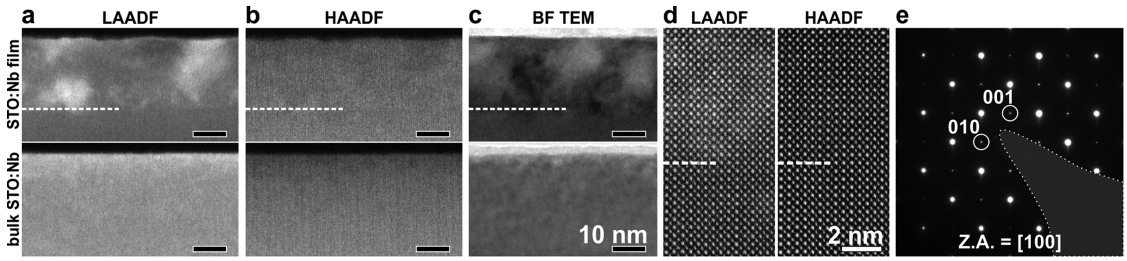

Figure 2. STEM ADF images simultaneously obtained from STO:Nb films and STO:Nb bulk crystals (a) using a LAADF detector with α_{adf} of about 20 mrad for strain imaging and (b) using a HAADF detector with α_{adf} of about 60 mrad for *Z*-contrast imaging. (c) Conventional BF TEM images from the same samples. (d) Atomic-resolution STEM LAADF and HAADF images of the STO:Nb film. (e) A SAED pattern recorded from the STO:Nb film. Interfaces between film (top) and substrate (bottom) are indicated by the dotted lines and the scale bars (a−c) represent 10 nm.

STEM ADF imaging is often considered a technique for visualization of structure with just atomic number sensitivity (*i.e.*, *Z*-contrast), this approximation is only valid when the ADF detector inner angle (α_{adf}) is considerably larger than the incident beam convergent semi-angle (α_{obj}), typically such that $\alpha_{adf} > 3 \times \alpha_{obj}$,[18,19] allowing for use of the Rutherford scattering model.[16,20] In cases where α_{adf} is not this large, overlapping and interfering diffracted beams reach the ADF detector and pure *Z*-contrast imaging is compromised (see Methods section and Supporting Information). This is ideal for detection of local lattice strain however.[17,21] Following this, Figure 2a,b shows side-by-side simultaneously recorded LAADF and high-angle ADF (HAADF) images of both thin film (top panels) and bulk crystal (bottom panels) samples. Note that the slight contrast changes in HAADF images across the films are due to thickness variations caused by TEM specimen preparation. The clear absence of bright regions in HAADF film images is an indication that those regions are indeed the result of localized lattice strain, not strong compositional variations. This conclusion is further supported by bright-field (BF) TEM imaging (Figure 2c) which also reveals contrast variations characteristic of strain but only in film samples.[22] None of these variations occur in bulk single crystal samples. As discussed in more detail below, the considerable quantities of interstitial Nb in these regions are the source of this strain. Atomic-resolution STEM ADF images (Figure 2d) also show contrast variations in the film samples, but critically, no evidence of microstructural changes or secondary phase formation in the strained high Nb content regions. Selected-area electron diffraction (SAED) patterns recorded from the same interfacial regions (Figure 2e) show no additional spots, and no distortions of the [100] pattern, ruling out secondary phases such as binary Nb oxides and $SrNbO_3$, which has the same crystal structure with slightly different lattice parameter,[23,24] a = 4.04 Å (see Supporting Information). SAED measurements in fact rule out $SrTi_{1-x}Nb_xO_3$ with $x > 0.3$. Since no systematic changes in oxygen content were observed, the observed strain is also unlikely to be associated with oxygen vacancies.[17] As discussed above, XRD measurements on such STO:Nb films indicate an average out-of-plane lattice parameter of 3.941 Å, 0.91% increased over the bulk STO lattice constant of 3.905 Å (see Supporting Information). This is consistent with an increase in unit cell volume due to Nb interstitials, which must be accommodated primarily by out-of-plane expansion due to the observed pseudomorphic growth (see Supporting Information for details). This expansion is expected to be nonuniform given that we have clearly observed nonuniform Nb interstitial density.

To evaluate the effects of interstitial Nb on the electronic properties of these STO:Nb films, EEL spectra at the Ti $L_{2,3}$ and O *K* edges were recorded as they probe the partial electronic DOS. Since we have demonstrated that Nb interstitials are accompanied by significant lattice strain, we first considered possible strain effects on this DOS. In the undoped STO substrates, where no Nb is present, EEL spectra at the Ti $L_{2,3}$ edge (Figure 3) were recorded both from typical unstrained regions, and from strained regions, intentionally generated during specimen preparation (see Supporting Information). As can be seen from Figure 3b, the differences in the Ti $L_{2,3}$ edges in strained and unstrained regions occur only in total intensity, not in fine structure (Figure 3c). This indicates that no detectable changes in DOS occur in the STO lattice at these strain levels, which are comparable with those observed in STO:Nb films (see Supporting Information for more details). We ascribe the overall intensity changes to dechanneling and broadening of the incident beam,[25] due to strain. Note that the slight anticorrelation of STEM LAADF and HAADF images in highly strained regions, as can be seen in Figure 2a,b, is also due to strain-induced changes in electron beam channeling.

Similar low-noise EEL Ti $L_{2,3}$ and O *K* edge spectra were acquired from STO:Nb films (with both substitutional and interstitial Nb) and from bulk STO:Nb crystals (with predominantly substitutional Nb) (Figure 4). Spectra from undoped STO substrates were also obtained for reference. Focusing first on the left panel of

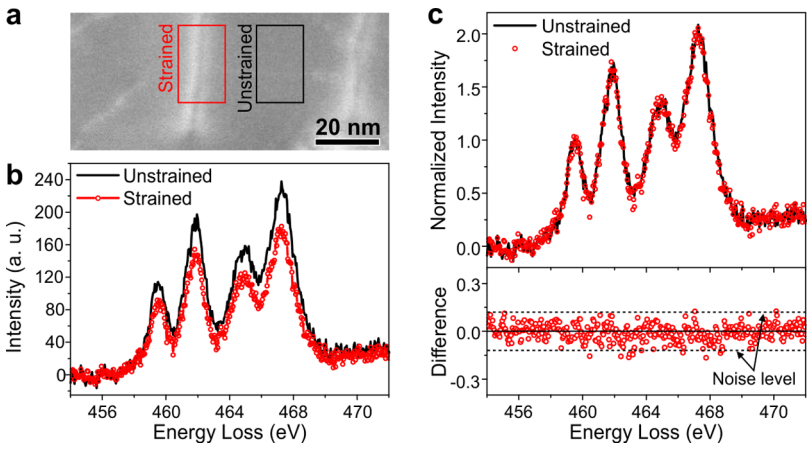

Figure 3. (a) STEM LAADF image of a STO(001) substrate with strained regions. The strain fields here originate from defects formed during ion milling. (b) Ti $L_{2,3}$ edge EEL spectra from unstrained and strained STO regions (areas of data collection are indicated in panel a by the black and red rectangles respectively). (c) Data in panel b after normalization. The difference between the normalized spectra is shown on the bottom, and statistical noise levels are indicated by the dotted lines.

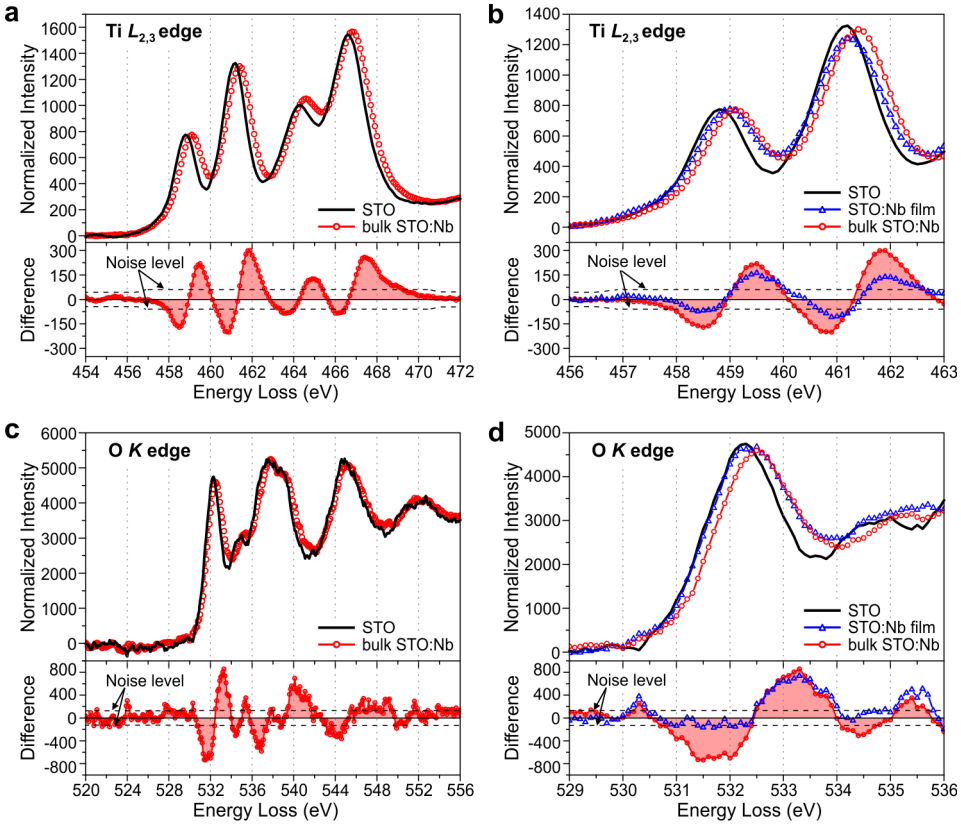

Figure 4. EELS fine structure of (a and b) Ti $L_{2,3}$ and (c and d) O *K* edges from undoped STO substrate, bulk STO:Nb with substitutional Nb doping, and STO:Nb film with substitutional and interstitial Nb. Differences with respect to undoped STO are shown on the bottom, and statistical noise levels are indicated by the dotted lines.

Figure 4, we see that the Ti $L_{2,3}$ and O *K* edges of bulk STO:Nb show a shift in the edge onsets, and additional changes in fine structure, relative to undoped bulk STO. This shift of 0.3 $\pm$ 0.05 eV in both Ti $L_{2,3}$ and O *K* edge onsets (Figure 4a,c) can be interpreted as an upward shift in the Fermi energy at 1.4 at. % substitutional Nb doping cf. nominally undoped STO, although it should be noted that this shift propagates throughout the fine structure, meaning that alterations of the DOS are also occurring, as opposed to rigid-band filling. Turning to the right panel of Figure 4, we see that the Ti $L_{2,3}$ and O *K* edge EEL spectra obtained from STO:Nb films show considerably smaller Nb-induced shifts in the edge onset region than bulk single crystal STO:Nb. This clearly suggests that Nb doping with a large density of Nb interstitials has a much weaker impact

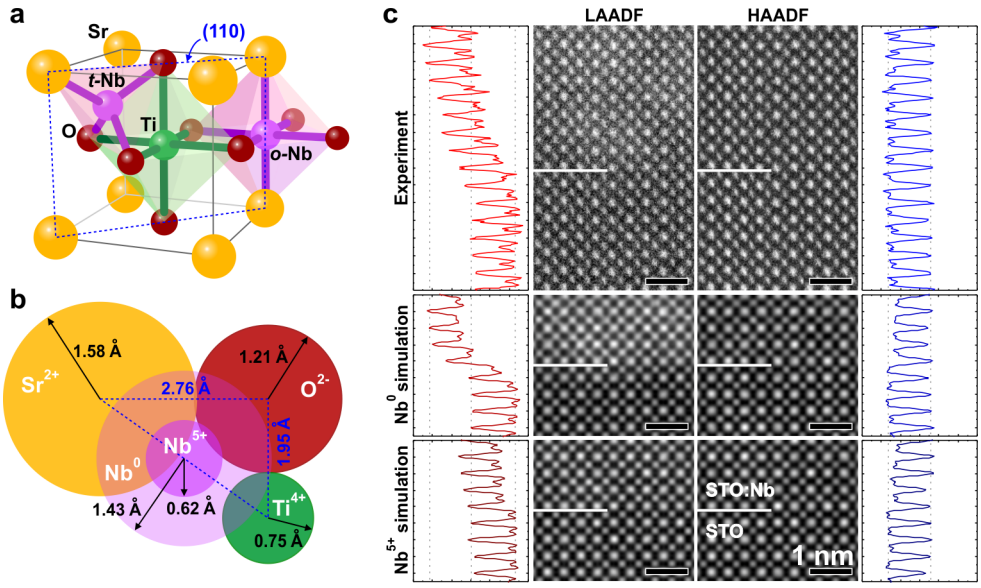

Figure 5. (a) Perspective view of the STO unit cell with interstitials (one *t*-Nb and one *o*-Nb), and a highlighted (110) plane (dotted blue line). (b) 2D schematic of the (110) plane in panel a showing a *t*-Nb interstitial overlapping with neighboring ions based on a hard sphere model. Ionic and/or atomic radii are the following: 12-coordinated Sr^{2+} (158 pm), 6-coordinated Ti^{4+} (74.5 pm), 2-coordinated O^{2-} (121 pm), 4-coordinated Nb^{5+} (62 pm), and Nb^{0} (143 pm).[26] (c) Comparison of STEM LAADF (left panel) and HAADF (right panel) images with corresponding intensity profiles obtained from experimental measurement (top, close-ups of Figure 2d), Nb^{0} simulation (middle), and Nb^{5+} simulation (bottom). The interfaces between film and substrate are indicated by the lines and the scale bars represent 1 nm.

on the band filling and distortion, *i.e.,* that these Nb interstitials are significantly less electronically active than substitutional Nb. As returned to below, we should emphasize that carrier compensation by other defects is also certainly possible. This is of course consistent with the vastly different electronic transport properties of bulk STO:Nb and these particular epilayers. Bulk STO:Nb crystals at this doping level have resistivity in the 10^{-3} Ωcm range at 300 K, compared to >100 GΩ resistance in these particular STO:Nb films. At higher energies (>459 eV for the Ti $L_{2,3}$ edge and 532.5 eV for the O *K* edge) significant changes in fine structure occur for STO:Nb films compared to both STO:Nb crystals and undoped STO. This indicates that high densities of interstitial Nb do induce higher energy changes in the DOS, as expected. Note that the observation that Nb incorporation clearly impacts the Ti edge is unambiguous evidence that the Nb dopants are in atomic-scale proximity to Ti ions, again confirming that precipitation of Nb-containing secondary phases does not occur.

Figure 5a shows, schematically, two obvious possible locations for interstitial Nb in the STO unit cell; one a tetrahedral site (*t*-Nb) and one an octahedral site (*o*-Nb). Each unit cell has 8 identical tetrahedral and 3 identical octahedral sites. A simple 2D hard sphere representation with Sr^{2+}, O^{2-}, Ti^{4+}, and *t*-Nb in a (110) plane is presented in Figure 5b, with the ionic radii[26] shown. The high compatibility of Nb^{5+} as a substitutional dopant on the Ti^{4+} site is simply seen from the similarity of the 6-fold coordinated ionic radii for Ti^{4+} (74.5 pm) and Nb^{5+} (78.0 pm).[26] Figure 5b also clearly shows that when Nb occupies interstitial sites (either *t* or *o*), it necessarily expands the local lattice parameter, introducing strain. The magnitude of this strain will depend on the oxidation state of the interstitial Nb, as aptly demonstrated by the comparison of the Nb^{5+} and Nb^{0} extreme cases in Figure 5b. Since the effective sizes of *t* and *o* interstitial sites are similar, the strain is expected to be similar in these two cases (see Supporting Information for details). Thus, for simplicity, we limit further discussion to *t*-Nb. It should be noted here that more study, beyond the scope of this report, will be necessary to clarify which of these two interstitial sites is energetically favorable for Nb.

To make quantitative comparison to the strain-sensitive high-resolution STEM LAADF images presented above, we constructed a simple model to estimate strain fields based on local Nb interstitial density, and the oxidation state of the interstitial Nb. Using a hard sphere model, the displacements of the first nearest neighbor Sr^{2+}, O^{2-}, and Ti^{4+} ions were first estimated around a Nb interstitial. The displacements of the second, third, fourth, *etc.* nearest neighbor ions were then evaluated through a displacement vector, $\vec{u}(\vec{r}) = (R_0^2 \delta R / r^3)\vec{r}$, at point $\vec{r}$ from the Nb interstitial site, where R_0 and δR are the distances and the displacements of the first nearest neighbor ions.[27] The strain field thus calculated was then used to simulate STEM LAADF and HAADF images using the *Multislice* computational method[28−30] with the code developed by Kirkland[31]

(see Supporting Information for details). Two sets of simulations were performed. In one case, all interstitial Nb was considered to be Nb^0, while in the second, all interstitial Nb was considered to be Nb^{5+}. To directly compare to experimental observations, we simulated 11.5 at. % Nb concentrations with 25% interstitial Nb, *i.e.*, the physical situation occurring in the nanoscopic region A in Figure 1a. A specimen thickness of 35 nm was considered here, to correlate with the actual specimen thickness measured experimentally using low-loss EELS (the log ratio method was used, with a mean free path for bulk plasmon generation in STO of λ_p = 123 nm).[32,33] The results are shown in Figure 5 both as images, and as laterally averaged intensity profiles. Clearly, the experimental STEM LAADF images and line profiles are in much closer agreement with the interstitial Nb existing in the Nb^0 state, broadly consistent with the EELS data. Partially ionized Nb (Nb^{4+} or Nb^{3+}) results in strain somewhat similar to that induced by Nb^{5+} (see Supporting Information), which is at much lower levels than that detected in experiment. In totality our microscopy and spectroscopy results thus point to substantial electrically inactive interstitial Nb^0 incorporation, consistent with the lack of metallic conductivity. Since Ti and Sr contents also fluctuate on the nanoscopic level, as shown in EDX data, Ti or Sr vacancy-driven compensation (and mobility reduction) may well also occur,[12] although this appears smaller than for Nb interstitials. Furthermore, since the Ti loss in the film is not uniform, the substituting Nb must clearly be clustered, likely further contributing to poor conductivity. In any case, we propose that defects and strain severely hinder the mobility in films such as these, precluding measurable electronic conductivity despite the fact that some substitutional doping does occur.

CONCLUSIONS

In summary, we have studied the local structural and electronic properties of STO:Nb epilayers deposited under conditions that yield nominally ideal stoichiometry for undoped STO. Even under such conditions, we find expanded out-of-plane lattice parameter, and insulating electronic behavior, in stark contrast to bulk Nb-doped single crystals. The Nb incorporation was found to be highly inhomogeneous on nanoscopic length-scales, the spatial variations being closely correlated to LAADF intensity in STEM imaging, which we demonstrate to be due to large quantities of interstitial Nb. Secondary phase formation is ruled out, even at the nanoscopic level. EEL spectra reveal changes in the DOS in STO:Nb films compared to undoped STO, but without the clear shift in the Fermi edge seen in bulk single crystal STO:Nb. From simple simulations, we argue that the strain field seen in experiments likely arises from interstitial Nb in the Nb^0 state. The results thus point to the presence of electrically inactive Nb interstitials in large quantities, which, in addition to other defects, are responsible for the poor bulk conductivity.

METHODS

Preparation of STO:Nb Films. In this work, 270 Å thick epitaxial STO:Nb films were deposited on STO(001) substrates by RF high pressure oxygen reactive sputtering from a 5 at. % Nb compound target synthesized by solid-state reaction/sintering. Prior to growth, substrates were annealed in 1.88 Torr of oxygen at 900 °C. Deposition was performed at 900 °C in 1.88 Torr of oxygen, followed by cooling in 600 Torr of oxygen. This was done at growth conditions optimized for undoped STO homoepitaxy, leading to identical lattice parameters for film and substrate, and vanishing X-ray scattering contrast (see Supporting Information for details). Although calibrated X-ray photoelectron spectroscopy confirms approximately 5 at. % Nb incorporation in the STO:Nb films, we obtain no measurable conductivity (*i.e.*, two-terminal resistance >100 GΩ), and out-of-plane lattice parameter of 3.941 Å, *i.e.*, 0.91% expanded over bulk STO (see Supporting Information). The data presented in this paper are for 5 at. % Nb films, although similar results were obtained from 0.1 to 5 at. % Nb and for thicker films, above any anticipated depletion thickness. For comparison, we also studied commercial (MTI Corporation) bulk single crystal undoped STO and STO:Nb, with 1.4 at. % Nb. Such doped crystals have close to 100% electrically active dopants, with negligible compensation.[1]

Characterization. Conventional TEM, STEM ADF imaging, and EELS data were acquired using a FEI Tecnai G2 F30 S-TEM equipped with a Gatan Enfina-1000 EEL spectrometer.[34] Additional EDX maps and STEM ADF images were obtained using aberration-corrected FEI Titan G2 80−200 and JEOL JEM-ARM200F STEM systems. Cross-sectional TEM specimens were prepared by a standard mechanical wedge polishing technique[35] followed by gentle ion milling (see Supporting Information for details). The EELS Nb $M_{2,3}$ edge has sharp white lines and is sensitive to oxidation state.[36,37] However, it has very small scattering cross section limiting its measurement in STO with proper signal-to-noise ratio without damaging specimens. Unfortunately, Nb $M_{4,5}$ edge with reasonably high scattering cross-section has delayed and fairly featureless fine structure,[37,38] limiting its usefulness for quantitative EELS (see Supporting Information). Detection of Nb was thus carried out using the new generation high-efficiency EDX systems available on modern aberration-corrected STEM systems. These systems allow higher X-ray count rates, and better sensitivity to low concentration elements. In our experiments, EDX composition maps were acquired in parallel from the Nb *L*, Ti *K*, O *K*, and Sr *L* peaks, with corresponding STEM ADF images. All data were recorded in a single scan, covering both film and substrate, and were repeated several times to ensure reproducibility.

Control of ADF Detector Inner Angle. To separate strain effects from *Z*-contrast in STEM ADF images, and to obtain solely *Z*-contrast information, the α_{adf} was controlled in STEM imaging. An FEI Tecnai G2 F30 S-TEM was used in these experiments. The α_{adf} can be controlled by varying the camera length. The strain contrast is seen to disappear with the increase of α_{adf} (*i.e.*, decreasing the camera length). The α_{obj} of the incident STEM probe was measured to be 9 mrad. We observed that HAADF images obtained with an $\alpha_{adf} \sim 60$ mrad is sufficient for *Z*-contrast imaging. For the same camera length, the inner angle of the LAADF detector is $\alpha_{adf} \sim 20$ mrad, which easily captures strain in the crystal (see Supporting Information).

Core-Loss EELS Measurements. EELS data were acquired using a FEI Tecnai G2 F30 S-TEM equipped with an Enfina-1000 Gatan spectrometer. Measurements were conducted with a dispersion of 0.05 (see Supporting Information) and 0.1 eV/channel at 200 kV. To prevent electron beam damage of the samples, and to increase signal-to-noise ratio of the EELS core-edges, 25−50 spectra for each sample were recorded, position-by-position, and the spectra were summed after aligning precisely to the zero-loss peak position. It was confirmed that the beam dwell time used in these experiments was sufficiently low to avoid detectable specimen damage. All spectra were recorded under the same conditions. Background signals were subtracted using a power-law fitting function and then EELS core-edges were normalized in the postedge region, *i.e.,* around 472 and 556 eV for Ti $L_{2,3}$ and O *K* edges, respectively.

Conflict of Interest: The authors declare no competing financial interest.

Acknowledgment. This work was supported partially by the MRSEC Program of the National Science Foundation under Award Number DMR-0819885, and the Abu Dhabi-Minnesota Institute for Research Excellence (ADMIRE), a partnership between the Petroleum Institute of Abu Dhabi and the Department of Chemical Engineering and Materials Science of the University of Minnesota. Work by P.A. and C.L. was also supported in part by the NSF under DMR-0804432. The authors would like to thank FEI Co and JEOL for their help with some of the experiments. We also thank Y. C. Park and J.-M. Yang in the National Nanofab Center (NNFC) in Republic of Korea for the assistance with EDX map, and C. Chung for the assistance with creating a supercell for the multislice STEM simulation.

Supporting Information Available: Details on XRD, EDX, EELS, and STEM experiments and multislice simulations. This material is available free of charge *via* the Internet at http://pubs.acs.org.

REFERENCES AND NOTES

1. Spinelli, A.; Torija, M. A.; Liu, C.; Jan, C.; Leighton, C. Electronic Transport in Doped $SrTiO_3$: Conduction Mechanisms and Potential Applications. *Phys. Rev. B* **2010**, *81*, 155110.
2. Kozuka, Y.; Susaki, T.; Hwang, H. Y. Vanishing Hall Coefficient in the Extreme Quantum Limit in Photocarrier-Doped $SrTiO_3$. *Phys. Rev. Lett.* **2008**, *101*, 096601.
3. Lin, X.; Zhu, Z.; Fauqué, B.; Behnia, K. Fermi Surface of the Most Dilute Superconductor. *Phys. Rev. X* **2013**, *3*, 021002.
4. Ohtomo, A.; Hwang, H. Y. A High-Mobility Electron Gas at the $LaAlO_3/SrTiO_3$ Heterointerface. *Nature* **2004**, *427*, 423–426.
5. Kozuka, Y.; Kim, M.; Bell, C.; Kim, B. G.; Hikita, Y.; Hwang, H. Y. Two-Dimensional Normal-State Quantum Oscillations in a Superconducting Heterostructure. *Nature* **2009**, *462*, 487–490.
6. Jalan, B.; Stemmer, S.; Mack, S.; Allen, S. J. Two-Dimensional Electron Gas in δ-Doped $SrTiO_3$. *Phys. Rev. B* **2010**, *82*, 081103.
7. Brinkman, A.; Huijben, M.; van Zalk, M.; Huijben, J.; Zeitler, U.; Maan, J. C.; van der Wiel, W. G.; Rijnders, G.; Blank, D. H. A.; Hilgenkamp, H. Magnetic Effects at the Interface between Non-Magnetic Oxides. *Nat. Mater.* **2007**, *6*, 493–496.
8. Lee, Y.; Clement, C.; Hellerstedt, J.; Kinney, J.; Kinnischtzke, L.; Leng, X.; Snyder, S. D.; Goldman, A. M. Phase Diagram of Electrostatically Doped $SrTiO_3$. *Phys. Rev. Lett.* **2011**, *106*, 136809.
9. Moetakef, P.; Williams, J. R.; Ouellette, D. G.; Kajdos, A. P.; Goldhaber-Gordon, D.; Allen, S. J.; Stemmer, S. Carrier-Controlled Ferromagnetism in $SrTiO_3$. *Phys. Rev. X* **2012**, *2*, 021014.
10. Jalan, B.; Allen, S. J.; Beltz, G. E.; Moetakef, P.; Stemmer, S. Enhancing the Electron Mobility of $SrTiO_3$ with Strain. *Appl. Phys. Lett.* **2011**, *98*, 132102.
11. Son, J.; Moetakef, P.; Jalan, B.; Bierwagen, O.; Wright, N. J.; Engel-Herbert, R.; Stemmer, S. Epitaxial $SrTiO_3$ Films with Electron Mobilities Exceeding 30,000 $cm^2\ V^{-1}\ s^{-1}$. *Nat. Mater.* **2010**, *9*, 482–484.
12. Kozuka, Y.; Hikita, Y.; Bell, C.; Hwang, H. Y. Dramatic Mobility Enhancements in Doped $SrTiO_3$ Thin Films by Defect Management. *Appl. Phys. Lett.* **2010**, *97*, 012107.
13. Oh, D.-W.; Ravichandran, J.; Liang, C.-W.; Siemons, W.; Jalan, B.; Brooks, C. M.; Huijben, M.; Schlom, D. G.; Stemmer, S.; Martin, L. W.; *et al.* Thermal Conductivity as a Metric for the Crystalline Quality of $SrTiO_3$ Epitaxial Layers. *Appl. Phys. Lett.* **2011**, *98*, 221904.
14. Rodgers, J. L.; Nicewander, W. A. Thirteen Ways to Look at the Correlation Coefficient. *Am. Stat.* **1988**, *42*, 59–66.
15. Pennycook, S. J.; Boatner, L. A. Chemically Sensitive Structure-Imaging with a Scanning-Transmission Electron-Microscope. *Nature* **1988**, *336*, 565–567.
16. Pennycook, S. J. *Z*-Contrast STEM for Materials Science. *Ultramicroscopy* **1989**, *30*, 58–69.
17. Muller, D. A.; Nakagawa, N.; Ohtomo, A.; Grazul, J. L.; Hwang, H. Y. Atomic-Scale Imaging of Nanoengineered Oxygen Vacancy Profiles in $SrTiO_3$. *Nature* **2004**, *430*, 657–661.
18. James, E. M.; Browning, N. D. Practical Aspects of Atomic Resolution Imaging and Analysis in STEM. *Ultramicroscopy* **1999**, *78*, 125–139.
19. Xin, H. L.; Muller, D. A. Three-Dimensional Imaging in Aberration-Corrected Electron Microscopes. *Microsc. Microanal.* **2010**, *16*, 445–455.
20. Williams, D. B.; Carter, C. B. *Transmission Electron Microscopy: A Textbook for Materials Science*; 2nd ed.; Springer: New York, 2009.
21. Yu, Z.; Muller, D. A.; Silcox, J. Study of Strain Fields at *a*-Si/*c*-Si Interface. *J. Appl. Phys.* **2004**, *95*, 3362–3371.
22. Hirsch, P. B.; Howie, A.; Nicholson, R. B.; Pashley, D. W.; Whelan, M. J. *Electron Microscopy of Thin Crystals*; 2nd ed.; Krieger: New York, 1977.
23. Tomio, T.; Miki, H.; Tabata, H.; Kawai, T.; Kawai, S. Control of Electrical Conductivity in Laser Deposited $SrTiO_3$ Thin Films with Nb Doping. *J. Appl. Phys.* **1994**, *76*, 5886–5890.
24. García-Jaca, J.; Santos, J.; Insausti, M.; Arriortua, M. I.; Rojo, T. Synthesis, Structure, Spectroscopic and Transport Properties of $(Ba_{1-x}Sr_x)NbO_3$. *Mater. Res. Bull.* **1996**, *31*, 1551–1558.
25. Fitting, L.; Thiel, S.; Schmehl, A.; Mannhart, J.; Muller, D. A. Subtleties in ADF Imaging and Spatially Resolved EELS: A Case Study of Low-Angle Twist Boundaries in $SrTiO_3$. *Ultramicroscopy* **2006**, *106*, 1053–1061.
26. Barsoum, M. W. *Fundamentals of Ceramics*; Taylor & Francis: New York, 2003.
27. Morgan, T. N.; Maier, H. Strain Fields and the Apparent Size of Donor Ions in GaP. *Phys. Rev. Lett.* **1971**, *27*, 1200–1203.
28. Cowley, J. M.; Moodie, A. F. The Scattering of Electrons by Atoms and Crystals. I. A New Theoretical Approach. *Acta Crystallogr.* **1957**, *10*, 609–619.
29. Kirkland, E. J.; Loane, R. F.; Silcox, J. Simulation of Annular Dark Field STEM Images Using a Modified Multislice Method. *Ultramicroscopy* **1987**, *23*, 77–96.
30. Loane, R. F.; Xu, P.; Silcox, J. Thermal Vibrations in Convergent-Beam Electron-Diffraction. *Acta Crystallogr., Sect. A: Found. Crystallogr.* **1991**, *47*, 267–278.
31. Kirkland, E. J. *Advanced Computing in Electron Microscopy*; 2nd ed.; Springer: New York, 2010.
32. Egerton, R. F. *Electron Energy-Loss Spectroscopy in the Electron Microscope*; 3rd ed.; Springer: New York, 2011.
33. LeBeau, J. M.; Findlay, S. D.; Allen, L. J.; Stemmer, S. Quantitative Atomic Resolution Scanning Transmission Electron Microscopy. *Phys. Rev. Lett.* **2008**, *100*, 206101.
34. Behr, M. J.; Mkhoyan, K. A.; Aydil, E. S. Orientation and Morphological Evolution of Catalyst Nanoparticles During Carbon Nanotube Growth. *ACS Nano* **2010**, *4*, 5087–5094.
35. Voyles, P. M.; Grazul, J. L.; Muller, D. A. Imaging Individual Atoms Inside Crystals with ADF-STEM. *Ultramicroscopy* **2003**, *96*, 251–273.

36. Bach, D.; Schneider, R.; Gerthsen, D.; Verbeeck, J.; Sigle, W. EELS of Niobium and Stoichiometric Niobium-Oxide Phases—Part I: Plasmon and Near-Edges Fine Structure. *Microsc. Microanal.* **2009**, *15*, 505–523.
37. Ahn, C. C.; Krivanek, O. L. *EELS Atlas*; Gatan, Inc: Warrendale, PA, 1983.
38. Tao, R.; Todorovic, R.; Liu, J.; Meyer, R. J.; Arnold, A.; Walkosz, W.; Zapol, P.; Romanenko, A.; Cooley, L. D.; Klie, R. F. Electron Energy-Loss Spectroscopy Study of Metallic Nb and Nb Oxides. *J. Appl. Phys.* **2011**, *110*, 124313.